



## A sustainable route to manufacture refractory high entropy alloy of AlMoNbTaTiZr from metal powder produced in solid state

Deepan S. L. Xavier, Nicholas S. Weston, Ian Mellor & Masoumeh Faraji

**To cite this article:** Deepan S. L. Xavier, Nicholas S. Weston, Ian Mellor & Masoumeh Faraji (2025) A sustainable route to manufacture refractory high entropy alloy of AlMoNbTaTiZr from metal powder produced in solid state, European Journal of Materials, 5:1, 2588824, DOI: [10.1080/26889277.2025.2588824](https://doi.org/10.1080/26889277.2025.2588824)

**To link to this article:** <https://doi.org/10.1080/26889277.2025.2588824>



© 2025 The Author(s). Published by Informa UK Limited, trading as Taylor & Francis Group.



Published online: 04 Dec 2025.



[Submit your article to this journal](#)



Article views: 224



[View related articles](#)



[View Crossmark data](#)

# A sustainable route to manufacture refractory high entropy alloy of AlMoNbTaTiZr from metal powder produced in solid state

Deepan S. L. Xavier<sup>a</sup>, Nicholas S. Weston<sup>b</sup>, Ian Mellor<sup>c</sup> and Masoumeh Faraji<sup>a</sup>

<sup>a</sup>Research Centre for Manufacturing and Materials, Coventry University, Coventry, UK; <sup>b</sup>School of Chemical, Materials and Biological Engineering, The University of Sheffield, Sheffield, UK; <sup>c</sup>Materials Discovery Centre, Metalysis, Rotherham, UK

## ABSTRACT

To enhance efficiency and reduce CO<sub>2</sub> emissions in applications such as jet-engines, gas turbines, and nuclear powerplants, alloys that withstand high temperatures are essential. High entropy alloys (HEA) containing refractory elements offer superior high-temperature properties. One of these refractory high entropy alloys (RHEAs) is AlMo<sub>0.5</sub>NbTa<sub>0.5</sub>TiZr. There are challenges when manufacturing these compositionally complex alloys using conventional techniques since they have elements with very high (Nb, Ta, Mo), high (Zr, Ti) and lower (Al) melting temperatures, creating mixing and homogeneity issues in alloy preparation. The Fray-Farthing-Chen (FFC) Cambridge process directly creates RHEA's powders without melting, but these feedstocks require a suitable consolidation technique. In this work field-assisted sintering technique (FAST), a novel rapid sintering technique, was used to make parts from powder of this alloy produced in solid-state. Among the process parameters the consolidation temperature had a more profound effect on density. From studied temperatures 1400 °C with a dwell time of 15 minutes produced the highest density level. Such a manufacturing route, occurring at temperatures lower than traditional casting, increases sustainability, and produces a homogeneous microstructure leading to parts with uniform properties and enhanced in-service performance.

## ARTICLE HISTORY

Received 11 June 2025  
Revised 30 October 2025  
Accepted 9 November 2025

## KEYWORDS



Field Assisted Sintering (FAST); high entropy alloys (HEAs); powder characteristics; refractory elements; refractory high entropy alloys (RHEAs)

## 1. Introduction

There is a growing demand for advanced materials to work under extreme conditions including high temperature and corrosive environments. High entropy alloys (HEAs) are novel alloys with multiple, often 5 or more, main elements. Certain HEAs that contain refractory elements are known for exhibiting excellent properties at elevated temperatures when compared to Ni-super alloys (Senkov et al., 2010; 2018). Conventional refractory alloys show significant reduction in their strength at temperature above 800 °C (Senkov et al., 2018). However, refractory high entropy alloys (RHEAs) such as AlMo<sub>0.5</sub>NbTa<sub>0.5</sub>TiZr, strengthened by B2 solid solution (an ordered structure based on body-centred cubic -BCC- phase), have shown lower reduction in their high temperature properties at 1000 °C and above (Senkov et al., 2018). High strength at elevated temperatures, makes AlMo<sub>0.5</sub>NbTa<sub>0.5</sub>TiZr alloys attractive for fuel cladding where a peak temperature (NRC Draft REGULATORY GUIDE DG-1263,1263, 2014) can reach 1200 °C.

It has been shown by Khan et al. (2024) that RHEAs such as (TiNbZr)<sub>89</sub>(AlTa)<sub>11</sub> show pronounced strain-rate sensitivity. They have also demonstrated enhancements in yield and ultimate compression strengths at strain rates reaching up to 3.0 × 10<sup>3</sup>/s. Enhancements in mechanical properties were attributed not only to the activation of dislocation mechanisms, but also to the formation of the B2 phase and Al<sub>3</sub>Zr<sub>5</sub> precipitates, which significantly increased the alloy's strength at high strain rates (Khan et al., 2024) (yield strength of 1300 MPa at 3.0 × 10<sup>3</sup>/s).

Broad microstructural space of HEAs offers a significant opportunity for the development of diverse hierarchical microstructures and consequently, enhanced mechanical properties. For example, Wang

**CONTACT** Masoumeh Faraji  [ac4240@coventry.ac.uk](mailto:ac4240@coventry.ac.uk)  Research Centre for Manufacturing and Materials, Coventry University, Coventry, UK.

© 2025 The Author(s). Published by Informa UK Limited, trading as Taylor & Francis Group.

This is an Open Access article distributed under the terms of the Creative Commons Attribution License (<http://creativecommons.org/licenses/by/4.0/>), which permits unrestricted use, distribution, and reproduction in any medium, provided the original work is properly cited. The terms on which this article has been published allow the posting of the Accepted Manuscript in a repository by the author(s) or with their consent.

et al. (2024) used controlled thermomechanical processing (cold rolling and intermediate- temperature annealing) in  $\text{Al}_{0.3}\text{CoCrFeNi}$  HEA to engineer a heterogeneous microstructure of heterogeneous grains, twins, dislocations and B2 precipitates to enhance fatigue property. Their work shows that hierarchically heterogeneous microstructure presents greater flexibility in tuning fatigue properties of HEAs. Their microstructurally engineered HEA demonstrated an excellent fatigue resistance, achieving a fatigue ratio of approximately 0.31 at a stress ratio of 0.1, which is reported to exceed that of most HEA alloys documented (Wang et al., 2024).

RHEAs have the potential to achieve ultrahigh hardness through severe plastic deformation. This has been demonstrated for ZrHfNbTaW alloy (Dangwal & Edalati, 2025) which synthesised by arc melting into dual BCC phases and deformed by high-pressure torsion (HPT). HPT transformed the structure to a single-phase BCC, achieving an exceptional hardness of 860 HV. The authors credited this increase in hardness to the synergistic effects of significant lattice distortion, solution hardening, grain-boundary hardening, and dislocation hardening (Dangwal & Edalati, 2025).

To predict the formation and stability of single-phase HEAs and consequently propose novel alloys for specific applications, combinatorial algorithms and computational techniques have been developed, including Alloy Search and Predict (ASAP) (King et al., 2016). ASAP has recently been used to identify and develop RHEA candidates including VNbCrMo (Ferreirós et al., 2023) for nuclear applications and  $\text{Zr}_{35}\text{Ti}_{35}\text{Nb}_{20}\text{V}_5\text{Al}_5$  with low-density, high specific strength and high ductility potentially for aerospace and nuclear applications (Yousefian et al., 2025). Both these alloys were produced in the lab using electric arc melting. However, improved mechanical properties of  $\text{Zr}_{35}\text{Ti}_{35}\text{Nb}_{20}\text{V}_5\text{Al}_5$  were achieved using deformation processing (cold rolling) alongside recrystallisation treatments. The recrystallised  $\text{Zr}_{35}\text{Ti}_{35}\text{Nb}_{20}\text{V}_5\text{Al}_5$  showed high tensile strength and ductility with the strongest (annealed at 800 °C for 30 mins) having a 0.2% proof yield strength of 1030 MPa and the most ductile (annealed at 900 °C 30 mins) having a ductility of 11.6% (Yousefian et al., 2025).

Some HEAs, also known as compositionally complex alloys (CCAs), have shown better corrosion behaviour when compared to conventional cladding alloys (Senkov et al., 2018). Hence, as agreed by the world experts who attended Nuclear Energy Agency (NEA) workshop in 2021 (Nuclear Energy Agency, 2023) and investigated by other researchers (Moschetti et al., 2022), HEAs are a promising option for advanced nuclear applications as bulk structural materials or coatings. However, they also believe “the deployment of HEAs will require the development of reliable manufacturing processes to ensure their advanced properties” (Nuclear Energy Agency, 2023). Furthermore, excellent high-temperature properties (e.g. high strength at elevated temperatures), and competitive oxidation resistance (Senkov et al., 2014; 2016), make them potential candidates for aerospace, as well as nuclear power plant applications.

Arc-melting of RHEAs is the conventional route which has been used so far to study and develop novel RHEA compositions (Chen & Zhuo, 2023). Currently, it is not possible to scale up the process readily to manufacture RHEAs in an industrial scale using this conventional route. On the other hand, the production of RHEAs with powder metallurgy has the potential to produce a fine, equiaxed structure with no elemental segregation unlike casting (Xiong et al., 2023; Zhang et al., 2024).

In addition to that, near net shaped components can be manufactured from the powder metallurgy route. At first, the RHEA powders were generally alloyed through mechanical alloying (MA) and then subsequently subjected to Field Assisted Sintering (FAST), also known as spark plasma sintering (SPS). Mechanical alloying produces fine and uniformly alloyed powders. FAST process produces ultra fine grains within a short processing time and hence it is the most common method for the sintering of RHEA powders. The parts produced by FAST possess superior hardness and yield strength than their as-cast counterparts due to the fine dispersion of secondary phases (Martin et al., 2024). Weston et al. (2015) produced a 250 mm disc with 26 mm thickness utilising a large-scale FAST, demonstrating the ability of the process to produce industrial-scale parts.

The powders for the FAST process are generally obtained by mechanical alloying of powders produced through the gas-atomisation process. As an alternative method of powder production, the Fray-Farthing-Chen (FFC) Cambridge process was developed in 1997 (Chen, 2013). In this process, a  $\text{TiO}_2$  ore was directly converted into a pure Ti metal by utilising electro-chemical reduction in a

molten calcium chloride bath. More details regarding the history, background, and details of the FFC Cambridge process can be found in (Chen, 2013; Chen & Fray, 2020).

The FFC Cambridge process enables the direct production of the alloy powders from their constitutive ores with accurate elemental concentrations. Traditionally, the pure metal must be extracted from its ore. Then this pure metal is alloyed in a vacuum arc melter (melting route) or alloyed through ball milling before subjecting the powder to compaction and sintering (powder metallurgy route). The FFC Cambridge process alloys the metal directly from their ore thus reducing a two-step stage (extraction and alloying) into a single step.

In addition to this, since the FFC Cambridge process involves a solid state electro-chemical process it eliminates the need for melting. This advantage is invaluable when manufacturing alloys consisting of metals with extremely high melting points like Tantalum, Molybdenum and Niobium which possess melting points above 2000 °C. In addition to this, by reducing the number of steps in the manufacturing process and by utilising a solid-state process which requires less energy compared to the melting route, the CO<sub>2</sub> emissions can be substantially lowered. These advantages are particularly realised when manufacturing alloys with complex compositions, such as high-entropy alloys (HEAs).

Thus, the FFC Cambridge process offers a competitive advantage over other processes in terms of cost, time, energy efficiency, environmental impact, and alloy design flexibility. Therefore, by utilising the appropriate manufacturing routes and tailoring the microstructure to desired properties, these powders can be used for applications in aerospace and nuclear industries. In this paper, for the first time the production of RHEAs manufactured by the powders produced from the FFC Cambridge process is reported. The powder was subjected to the FAST process, where the role of the process parameters on the density, microstructure and properties is discussed.

## 2. Experimental

### 2.1. Materials

The general class of documented lightweight RHEAs, incorporating the AlMoNbTaTiZr system, which exhibits promising strength at elevated temperatures (Senkov et al., 2018), were selected for investigation, to demonstrate the viability of the solid-state electro de-oxidation technology of producing powders in volume. A criticism of these materials is that no clear route to scale is apparent. More traditional melt routes would encounter challenges in combining elements such as tantalum and aluminium, due to their disparate densities (a density difference of 14 g/cm<sup>3</sup> at room temperature) and melting temperatures (a melting temperature difference of 2336 °C).

To integrate molybdenum, the electro de-oxidation technique was adopted. In this process, oxidation state of the oxide, through initial selection or via reaction with other raw materials, can influence retention in the final alloy. The feedstock preparation conditions also directly influence the retention of elements in the final alloy (Bhagat et al., 2008). This has resulted in a lower molybdenum content in the HEA powder than intended, which will be addressed in future development activity.

The RHEA alloy (AlMoNbTaTiZr) used in this study was supplied by Metalysis Ltd and was produced using the FFC Cambridge process. The chemical composition of the powder, as determined by X-ray fluorescence (XRF) spectroscopy using samples from three distinct containers, is presented in Table 1. The data revealed the presence of minor impurities (including Ca, Cl, Hf, Si and Ni). Calcium and chlorine are introduced during the electrochemical reduction process; however, the other elements are present by being carried through from the starting metal oxides, which can be eliminated by sourcing feedstocks of certain purities. The powder size distribution was studied using the laser

**Table 1.** The average chemical composition of the powder determined from three XRF measurements with their standard deviation (Std.Dev.).

Elements	Al	Mo	Nb	Ta	Ti	Zr	Ca	Cl	Hf	Si	Ni	Fe
Ave. (Wt.%)	5.20	2.00	30.90	26.00	11.28	23.13	0.08	0.03	0.43	0.81	0.01	0.13
Std.Dev.	0.09	0.04	0.15	0.04	0.10	0.01	0.00	0.01	0.01	0.03	0.00	0.01
Target (Wt.%)	6.79	12.07	23.37	22.76	12.05	22.96						

diffraction technique through the Anton Paar PSA 990 particle size analyser. The finding of this part of the study is given in the results section under the “Powder characteristics” section.

## 2.2. Consolidation process

The powder was compacted and consolidated using an FCT Systeme GmbH Type HP D25 FAST furnace, based in the Henry Royce Institute at the University of Sheffield. To produce each test coupon, approximately 5.81 g of powder was placed between two graphite punches inside a 20 mm internal diameter graphite ring die. Initially, a 5 kN contact load was applied through hydraulic rams before evacuating the chamber to reach pressures below 0.01 mbar. An optical pyrometer measured and controlled the temperature, located about 5 mm from the centre of the upper sample surface. The samples, discs of 20 mm diameter by 2.5 mm thickness, were FAST-processed under various dwell temperatures, isothermal holding times at the sintering temperature, and heating and cooling rates.

A 50 MPa pressure was applied to all samples, with temperature and pressure rising together until reaching a peak, held for 15- or 30-min. Loading decreased while temperature reduced following a specific path. See [Figure 1](#) for cycles. Process conditions, and their relative density are summarised in [Table 2](#). Two reasonably high-density conditions (S5 and S7) were selected for replication to confirm reproducibility.

The relative density was derived as the physical volumetric density divided by the theoretical density. The volumetric density of the bulk samples was calculated by physical measurements, and

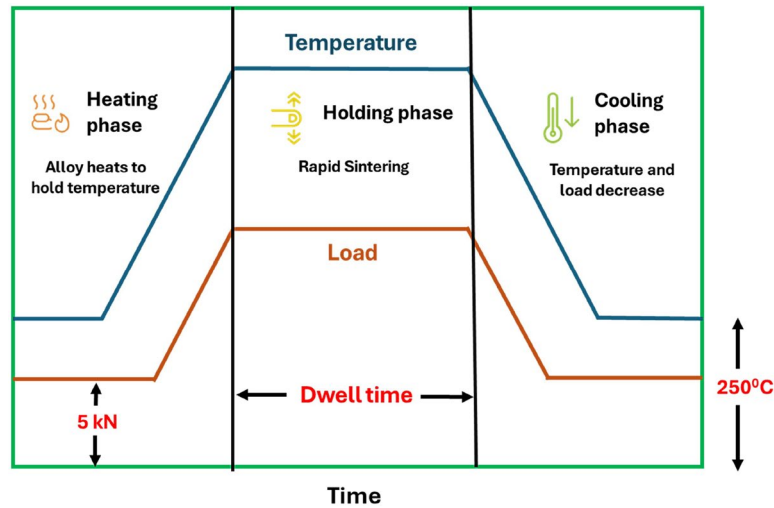


**Figure 1.** A typical heating and loading cycle in the FAST machine used here.

**Table 2.** The FAST consolidation conditions for each sample (uncontrolled cooling rate is approximately 200 °C/min), and their relative density.

Sample	Temperature (°C)	Holding Time (min)	Heating Rate (°C/min)	Cooling Rate (°C/min)	Relative Density (%)
S1	800	30	100	Uncontrolled	51.11
S2	1000	30	100	Uncontrolled	72.57
S3	1200	15	100	Uncontrolled	93.53
S4	1200	30	100	Uncontrolled	95.06
S5	1400	15	100	Uncontrolled	98.12
S6	1400	15	100	Uncontrolled	97.82
S7	1400	30	100	Uncontrolled	96.08
S8	1400	30	100	Uncontrolled	96.08
S9	1500	15	100	Uncontrolled	95.47
S10	1400	15	30	30	95.26
S11	1400	15	30	50	96.28
S12	1400	15	100	30	98.02
S13	1500	15	100	30	97.61
S14	1500	15	100	100	97.51

the theoretical density of the alloy was calculated as  $7.23 \text{ g/cm}^3$ , using the concentration dependent rule of mixtures equation given below (Eq. 1) where  $c_i$ ,  $A_i$  and  $\rho_i$  are the atomic fraction, atomic weight and density of element  $i$ , respectively (Senkov et al., 2010):

$$\rho_{mix} = \frac{\sum c_i A_i}{\sum c_i A_i / \rho_i} \quad (1)$$

### 2.3. Characterisation of FAST -processed samples

For microstructural characterisation the samples were prepared using standard metallographic techniques. Initially, the samples were grinded using SiC papers and subsequently polished by  $9 \mu\text{m}$ ,  $3 \mu\text{m}$  polycrystalline diamond suspensions followed by fine polishing using  $0.06\text{-micron}$  colloidal silica solution. The identification of porosities was carried out under the Nikon Eclipse LV150NL optical microscope.

X-ray diffraction (XRD) experiments were conducted using a Bruker D8 Advanced Diffractometer between  $20^\circ$  and  $90^\circ$  with Cu K $\alpha$  radiation ( $\lambda = 0.154 \text{ nm}$ ) operating at  $40 \text{ kV}$  voltage with a current of  $40 \text{ mA}$  and a step size of  $0.02^\circ$ . A Zeiss Scanning electron microscope (SEM), Sigma 500 VP, equipped with energy dispersive spectroscopy (EDS) was used to study microstructure and map elemental distributions. Microhardness of samples was measured with Vickers technique using a Struers D80 Durascan-70 per ASTM E384 (ASTM E384-22, 2022), applying a  $200\text{-gf}$  load for 15 seconds. The spacings between the indents were at least 3 times the diameter of the indenter and a minimum of 5 indentations was performed per sample.

## 3. Results and discussion

### 3.1. Powder characteristics

The volume weighted size distribution in Figure 2 shows mostly  $20 \mu\text{m}$  diameter particles. Figure 2 shows  $D_v(10)$ ,  $D_v(50)$ ,  $D_v(90)$  diameters where 10%, 50% and 90% of particles fall below. The average mean size volume of the three samples is determined as  $23.92 \mu\text{m}$  using the software which uses Eq. 2 (Technical Note TN156 2021) based on ASTM E799 standard (ASTM E 799-03,03, 2020).

$$D[4,3] = \frac{\sum_1^n D_{ivi}^4}{\sum_1^n D_{ivi}^3} \quad (2)$$

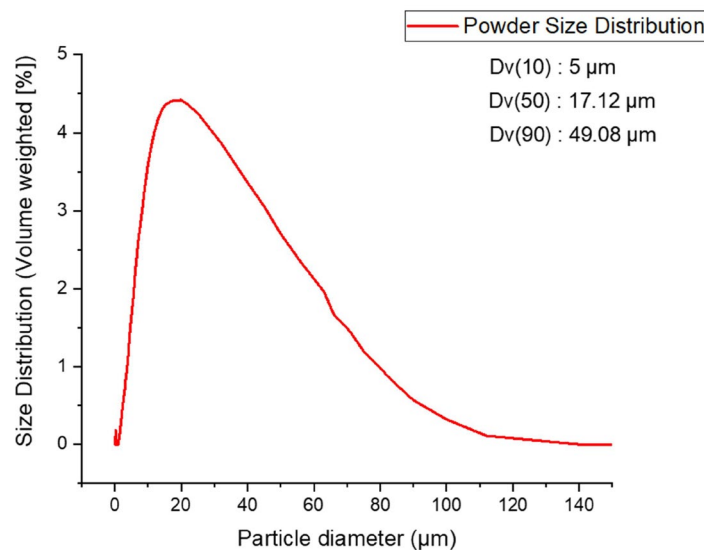


Figure 2. The volume weighted particle size distribution across different sizes.



where  $D[4,3]$  and  $D_i$  are the mean diameter over volume (Murty et al.) and the diameter of ith particle, respectively. More information on the software and the equation is found in (Technical Note, XXXX Technical Note TN156 2021). The span of powder distribution shows the distribution width of the particles between  $D_v(10)$  and  $D_v(90)$ . The span is calculated as  $2.57\mu\text{m}$  using Eq. 3 (Technical Note TN156 2021). Higher the span, higher is the distribution of particles across different sizes. When the span is closer to zero the particle size becomes homogeneous. The required powder particle span can vary for each manufacturing process. In this work, the span was situated between a narrow and broad particle size distribution range.

$$Span = \frac{D_{90} - D_{10}}{D_{50}} \quad (3)$$

The X-ray diffraction pattern of the powder (Figure 3) indicated the presence of a BCC phase and  $\text{Al}_3\text{Zr}_5$  intermetallic. Figure 4 represents the SEM secondary electron (SE) images of powder taken at different magnifications. The low magnification image reveals irregularly sized particles, while the high magnification image depicts agglomerated fine particles.

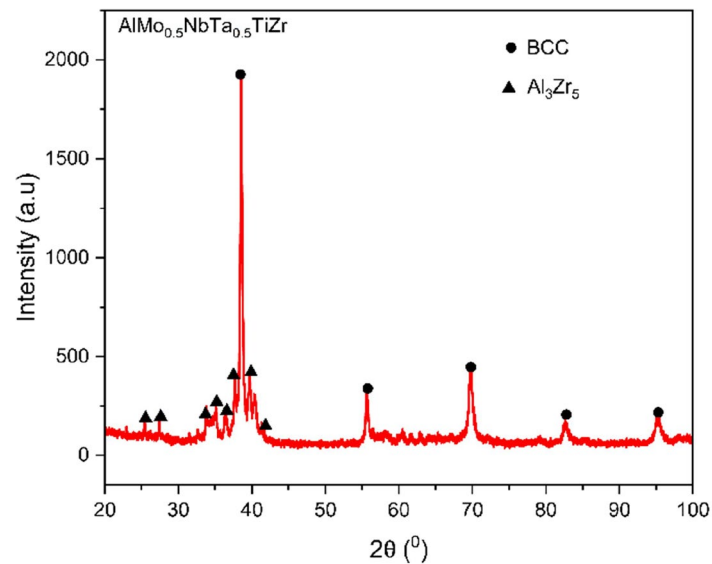


**Figure 3.** The XRD pattern of the powder.

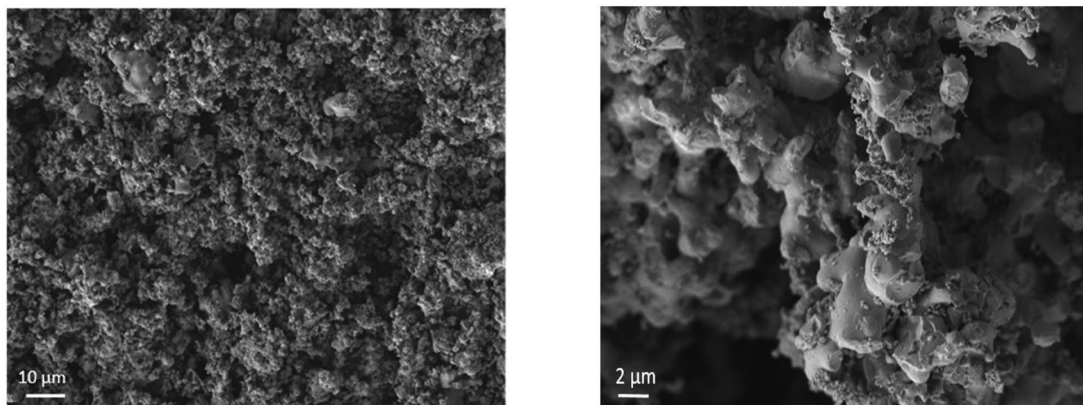


**Figure 4.** SEM images of the raw powder a) Low magnification b) High magnification.

### 3.2. FAST

#### 3.2.1. Chemical composition

To analyse the influence of processing on the chemical composition, the chemical composition of the samples processed by FAST were confirmed by XRF, which are summarised in Table 3. From Table 3, no significant differences were seen between the raw powder used and the FAST samples.

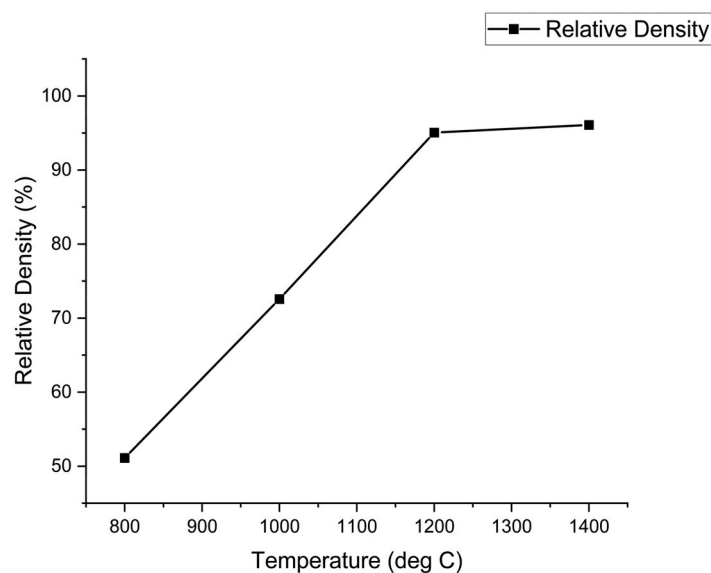
#### 3.2.2. The role of the process conditions on the density of the parts

Figure 5 plots the trend of relative density with increasing temperature for a regime consisting of heating rate of 100 °C/min, dwell time of 30 minutes, followed by uncontrolled cooling with an approximate cooling rate of 200 °C/min. The slope of the curve changes noticeably at 1200 °C. Between 800 °C to 1200 °C, the slope of the curve measures as 0.109; however, between 1200 °C to 1400 °C this slope is reduced to 0.015. These values demonstrate that up to 1200 °C the temperature plays a critical role in increasing the density, compared to temperatures beyond 1200 °C where the rate of densification decreases.

The effect of holding time on the relative density can be studied from Table 2. At 1200 °C, a longer holding time increases the relative density (S4 versus S3). In contrast to this, at 1400 °C, a longer holding time decreased the relative density of the samples by 1.5% (S7 versus S5). To confirm this result, the samples were reproduced, and similarly ~1% reduction was observed (S8 versus S6). The

**Table 3.** The chemical composition of the uncontrolled cooling samples (cooling rate of  $\approx 200$  °C/min) manufactured by the FAST process along with the powder.

Sample / Mass%	S1	S2	S3	S4	S5	S7	S9	Powder
Al	7.035	6.726	4.887	7.059	6.900	6.707	6.679	5.203
Si	0.755	0.724	0.835	0.879	0.750	0.839	0.769	0.811
Cl	0.049	0.0360	0.154	0.026	0.058	0.020	0.031	0.029
Ca	0.109	0.054	0.117	0.176	0.146	0.119	0.069	0.080
Ti	10.994	10.712	10.828	11.724	11.314	11.269	10.510	11.277
Fe	0.146	0.127	0.135	0.137	0.135	0.156	0.108	0.128
Zr	22.840	22.460	23.428	22.462	22.774	22.307	22.491	23.125
Nb	29.921	30.221	30.834	29.694	29.653	29.847	30.172	30.903
Mo	1.741	2.103	2.067	1.836	1.933	2.052	2.012	1.995
Hf	0.504	0.523	0.470	0.496	0.427	0.453	0.496	0.432
Ta	25.905	26.315	26.077	25.510	25.912	26.204	26.664	26.002



**Figure 5.** The evolution of relative density with respect to temperature for a regime consisting of heating rate of 100 °C/min, dwell time of 30 minutes, followed by uncontrolled cooling with an approximate cooling rate of 200 °C/min (uncontrolled cooling).



pores are usually located along the grain boundaries (as seen under SEM), and they migrate together with the grain boundaries. At higher temperatures, an increase in the holding time provides sufficient activation energy for the pores to migrate and coalesce with each other. The decrease in relative density observed might be due to the coalescence and growth of pores during such prolonged holding periods.

Sample S10 was manufactured with a heating rate of 30 °C/min compared with S12 with a heating rate of 100 °C/min. From Table 2, it can be shown that a faster heating rate enhanced the density. This is because slower heating rates allow more time for pore migration and coalescence. This may be down to the rapid heating rate bypassing the traditional initial stages of sintering where a network of interconnected pores is created and then broken up, trapping closed pores within the material. At high heating rates, the particles quickly become very soft and thus deform rapidly under the applied load. Particle deformation and rearrangement to fill voids could drastically reduce the trapped porosity within the material. Similar to the observation here, when sintering W-Fe-Ni powders, Hu et al. (2013) found that processing at lower sintering temperatures (<1200 °C), with slower heating rates increased the density, whereas higher sintering temperatures (>1200 °C) and higher heating rates densified the samples.

This study didn't investigate the effect of heating rates on densification; however, Hu et al. (2013) examined the role of heating rates at lower and higher temperatures on densification and measured the activation energies for the kinetics of densification. Their findings showed that mechanisms governing densifications for lower heating rates (below 100 °C/min) are influenced by grain growth occurring due to surface diffusion. Conversely, at higher temperatures (>1200 °C) and higher heating rates (above 100 °C/min), solution-precipitation and Ni-enhanced W grain boundary diffusion contribute significantly to densification, while grain-growth is minimised.

When analysing the equipment data, under this work, it was found that during uncontrolled cooling, high cooling rates of approximately 200 °C/min were developed. Overall, to identify the most optimum cooling rate, a few different cooling rates were examined. These conditions include cooling rates of 30, 100 and 200 °C/min (uncontrolled cooling) for two different dwell temperatures of 1400 and 1500 °C, at a fixed heating rate of 100 °C/min. From these experiments, a cooling rate of 30 °C/min gives the most optimum relative density (Table 2).

The optical micrographs in Figure 6 shows the reduction of porosity with increasing sintering temperature. This is in accordance with other FAST parameter studies (Cavaliere et al., 2019; Guillon et al., 2014). In Figure 6d and e, no significant difference is seen in the amount of porosity when increasing the holding time from 15 to 30 minutes. Thus, in general, the contribution of temperature to the improvement of relative density is significantly higher compared to the other FAST parameters.

Understanding of powder densification is critical in controlling the microstructure. The densification curves of all the samples are represented in Figure 7a and b. Relative density during FAST for each sample is obtained based on the final density determined by physical measurements and the displacement of the ram recorded during the experiment where the mass is constant.

The effect of heating rate on the densification rate is presented in Figure 7b. On this Figure, the legend 1400/30/30 indicates that the alloy was sintered at 1400 °C with a heating and cooling rates of 30 and 30 °C/min. Although, a slower heating rate has shown a slightly lower densification rate, the differences in the final density are minimal.

Figure 8 provides a comparison of relative density variation and temperature with time for two different samples with different heating rates a) 100 °C/min and b) 30 °C/min with the same sintering temperature (1400 °C) and the same cooling rate (30 °C/min).

Figures 7 and 8 demonstrate that during all the studied conditions the increase in relative density follow a sigmoidal trend.

From Figure 8, it can be inferred that there are three stages of densification: I) Initial stage, where no densification occurred during heating; II) Rapid densification stage, where high densification rates are observed. During this stage, the densification begins here at approximately 760 °C for both conditions; III) Final stage, where little or no densification occurs during holding at high temperature. Both images (8a and 8b) show that during the second stage a major part of the densification occurs,

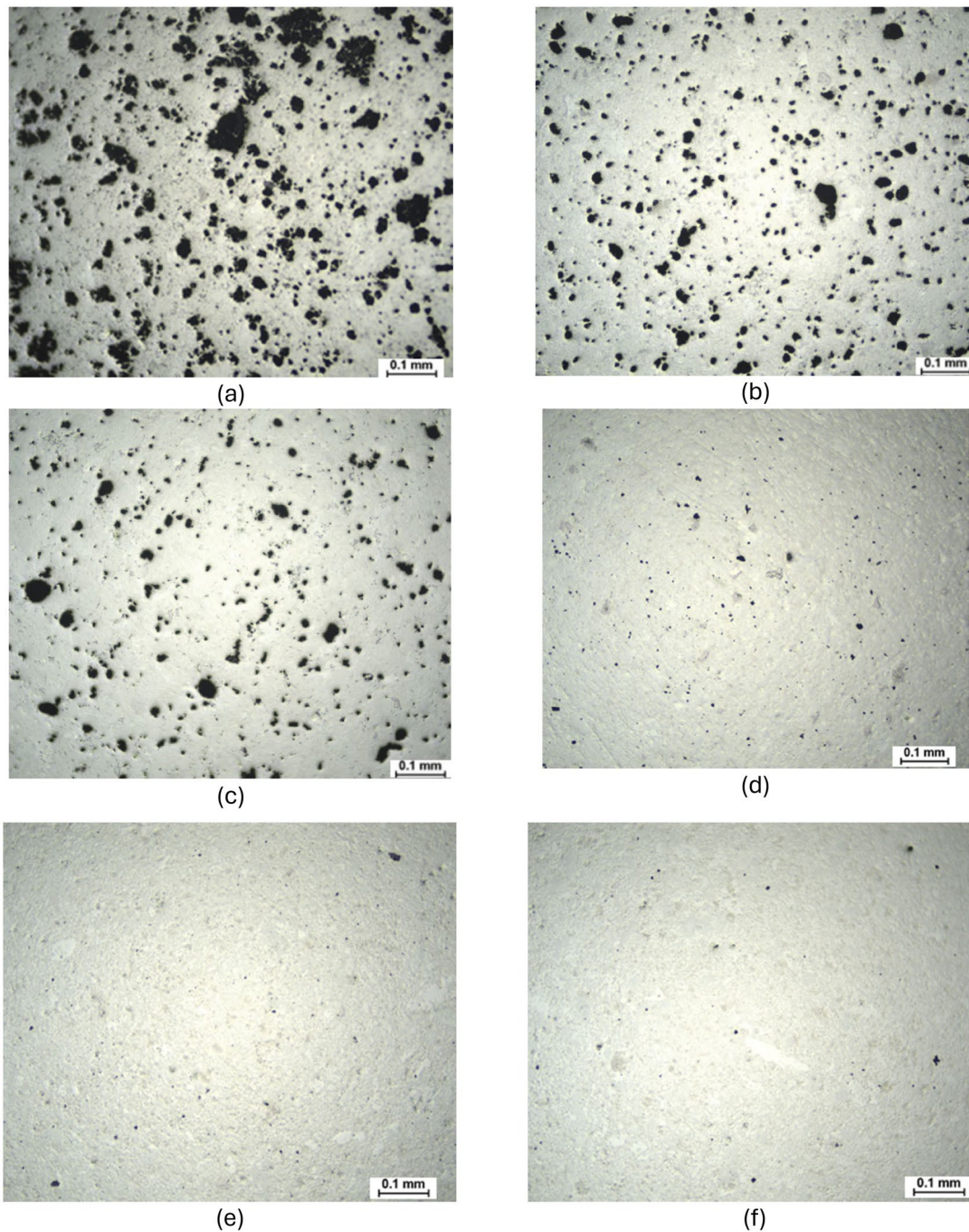


**Figure 6.** Optical micrographs of the FAST samples with increasing temperature (a to f) a) 1000°C/30 min, b) 1200°C/15 min, c) 1200°C/30 min, d) 1400°C/15 min, e) 1400°C/30 min f) 1500°C/15 min.

when the temperature increases gradually in a controlled manner. When the maximum temperature is reached, the rate of densification slows down.

The alloy with a slower heating rate (shown in [Figure 8b](#)) showed gradual increase in density at the final stages but the alloy with a faster heating rate (shown in [Figure 8a](#)) showed little to no improvement in density at this stage. Interestingly, although the heating rates were different for both conditions, the onset of rapid densification for both alloys occurred at 760°C. This reemphasises the significance of sintering temperature on the densification process.

Other workers utilising SPS on commercial atomised copper powder (Diouf & Molinari, [2012](#)) and Ti-6Al-4V powders reinforced with TiN and TiCN (Falodun et al., [2019](#)) observed an initial increase in density before the rapid densification stage. This effect was attributed to the particle rearrangement

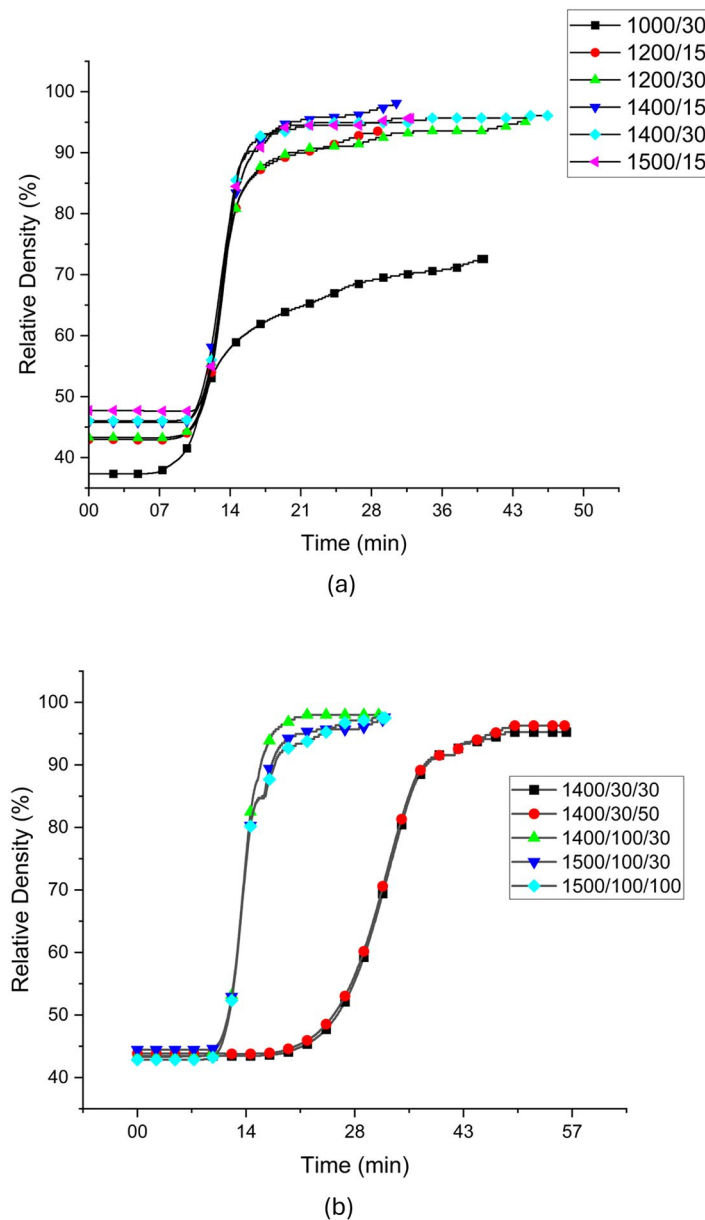


**Figure 7.** Density variations during the FAST with respect to time a) Samples with a heating rate 100°C/min and uncontrolled cooling. Legend shows the sintering temperature (°C) and the dwell time (min), respectively. b) Last 5 samples with different heating and cooling rates. Legend shows the sintering temperature, heating rate and the cooling rate (°C/min), respectively, all had 15 min dwell time.

during the initial densification stage. However, such a particle rearrangement effect, demonstrated by an initial sharp increase in density and their initial data can be collected by the SPS machine, was absent during the densification of this RHEA.

During powder densification, particle rearrangement refers to the movement of powder particles within the pressurised container which increases the density of the compact. This mechanism of densification is usually succeeded by the diffusion stage where densification occurs by neck formation and growth between powder particles promoting volume diffusion and grain boundary diffusion.

The absence of this particle rearrangement stage is due to the interatomic forces such as Van der Waals forces and surface tension between the powder particles due to their irregular morphology. This can also be attributed to the initial agglomeration of these powders. All these effects can be seen in the microstructure of the powder before pressing as seen in Figure 4. This means that the final microstructure is directly a product of the initial arrangement of the powder which could affect

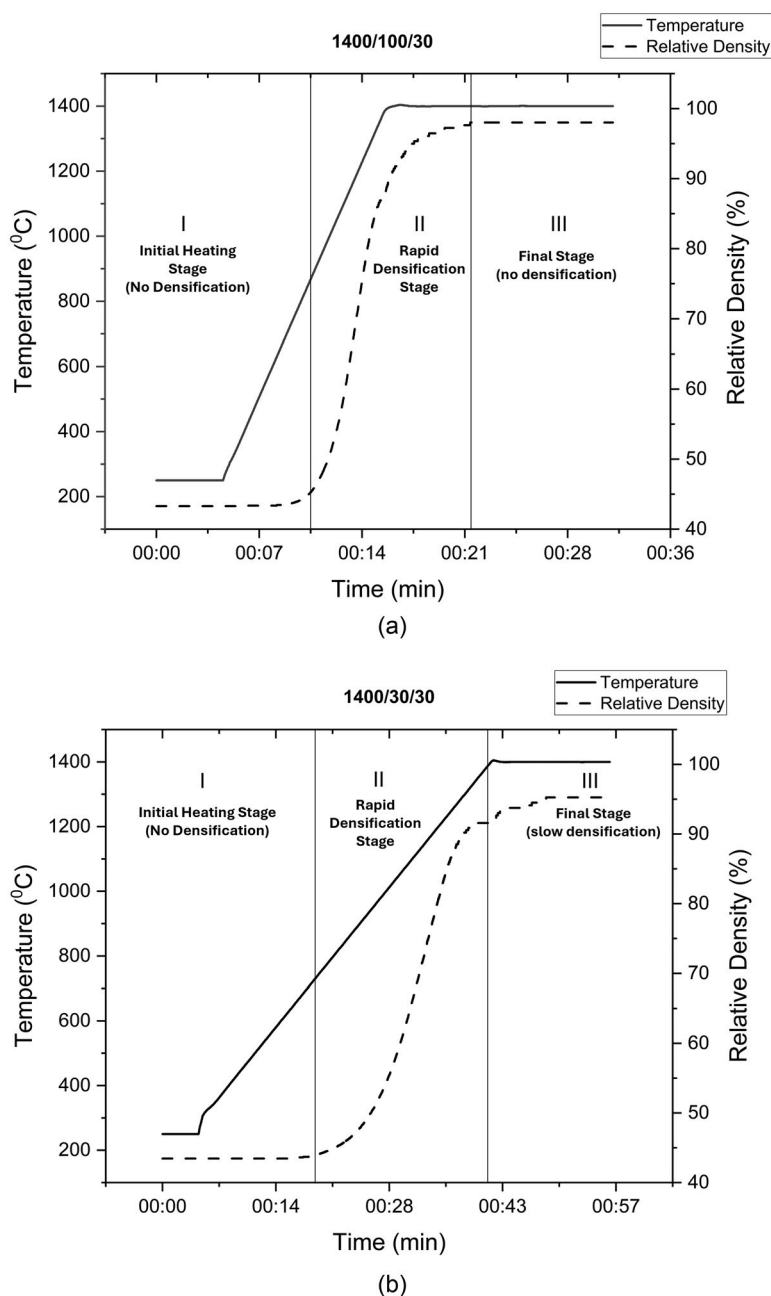


**Figure 8.** Variation of relative density and temperature with respect to time for samples sintered at 1400°C and a cooling rate of 30°C/min, samples with a heating rate of 30°C/min (a) and 100°C/min (b), depicting three stages of densification.

the microstructure and its properties. This also means that the main densification mechanism operating under FAST is based on volume diffusion and grain boundary diffusion through neck formation and growth between individual powder particles.

### 3.3. X-ray diffraction

X-ray diffraction (XRD) analysis was employed to identify the phases present in each FAST sample, with the corresponding diffraction patterns presented in [Figure 9](#). Irrespective of the processing conditions, all samples exhibited the presence of two primary phases: a body-centred cubic (BCC) phase and a hexagonal Al–Zr intermetallic phase, identified as  $\text{Al}_3\text{Zr}_5$ . Other researchers have reported formation of  $\text{Al}_3\text{Zr}_5$  when annealing  $\text{AlMoNbTaTiZr}$  alloys at about 1200°C (Whitfield et al., [2021a](#),



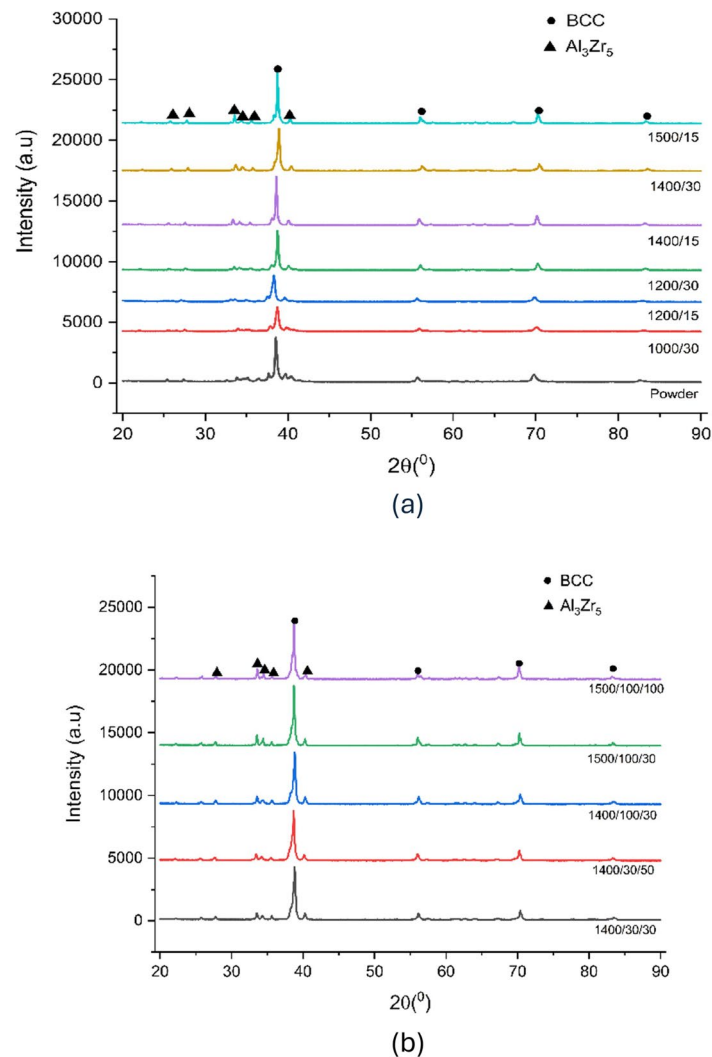


**Figure 9.** XRD plots of the samples manufactured at different FAST conditions a) The label below each plot indicates the sintering temperature ( $^\circ\text{C}$ ) and the holding time (min). All the samples had a constant heating rate of 100°C/min and a constant cooling rate of 30°C/min. b) The label below each plot indicates the sintering temperature ( $^\circ\text{C}$ ), the heating rate, and the cooling rate ( $^\circ\text{C}/\text{min}$ ), all with a constant holding time of 15 minutes.

2021b). Similar phase constituents were also observed in the as-received powders, indicating that no phase transformations occurred during the FAST process. This suggests that the role of FAST in this context was limited to densification rather than altering the phase constitution. Notably, the intensity of the BCC diffraction peaks increased significantly in samples sintered at temperatures exceeding 1400°C, correlating with the achievement of higher densification levels.

### 3.4. Microstructural observation

Figure 10 displays the SEM-BSE images for the samples manufactured at 1400 and 1500°C with varying holding time, heating and cooling rates. This figure shows a mixture of bright and dark phases in the microstructure of all samples.

The bright phase was found as the primary matrix phase exhibiting continuity. The grains had a granular nature and was homogenous throughout the microstructure. The dark phase had a blocky, angular, and irregular morphology and was partially connected in some areas.

The chemical composition of the bright and dark phases was determined by energy dispersive spectroscopy (EDS) through point scan technique, which is tabulated in Table 4. For the analysis

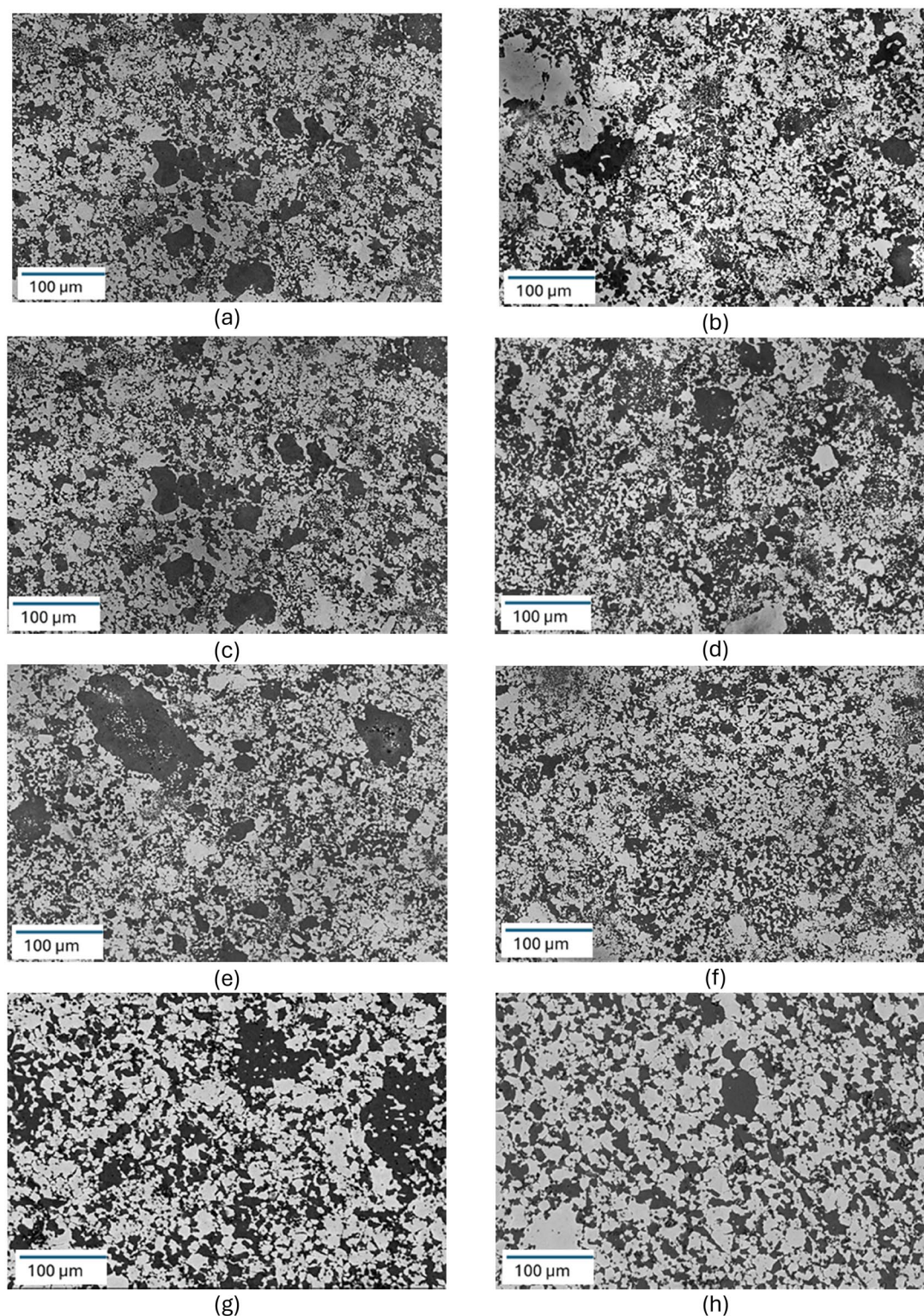


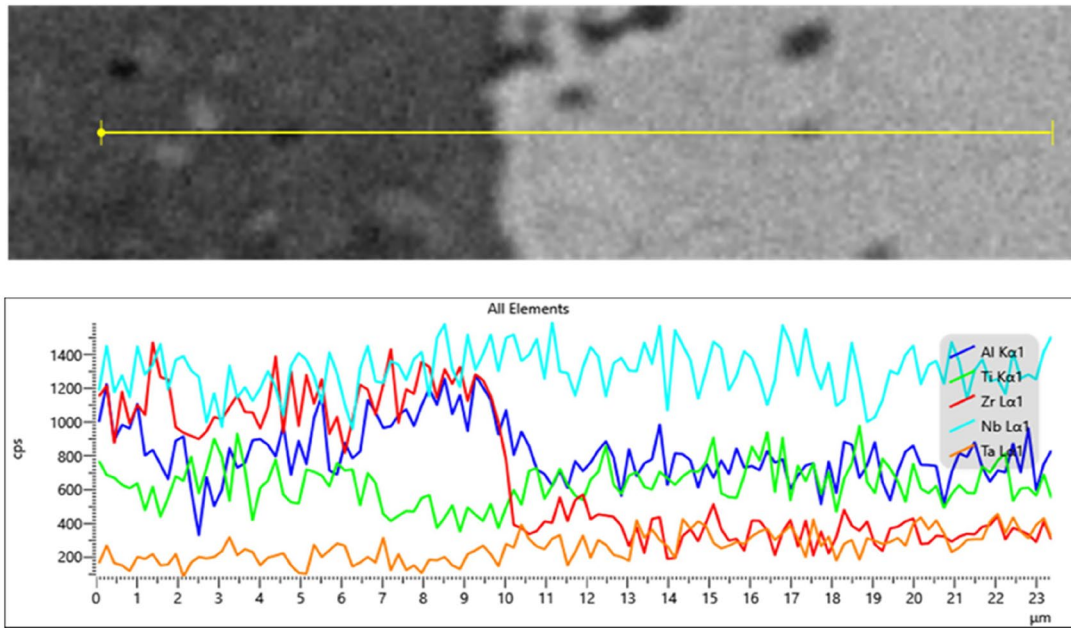
**Figure 10.** SEM-BSE images of the samples with maximum FAST density sintered at 1400 and 1500°C a) S5 b) S7 c) S9 d) S10 e) S11 f) S12 g) S13 h) S14 (Processing details are given in [Table 2](#)).

undertaken here, at least 5 points were chosen for each phase in the samples. From the EDS data, it can be inferred that the bright phase contains mainly Nb, Ti, Al and Ta with some Mo and Zr present. Thus, the bright phase is the BCC phase containing Nb, Ti, Al, and Ta in its crystal lattice. The dark phase has Zr and Al as the dominant elements followed by Nb and Ti in equal proportions.



**Table 4.** Elemental composition of the bright (B) and dark (D) phases for the samples sintered at 1400°C and 1500°C (Processing details are given in Table 2).

Element		S5	S7	S9	S10	S11	S12	S13	S14
Al	B	17.5±0.9	20.0±0.8	21.1±0.9	17.2±1.1	18.3±1.6	15.8±1.0	18.6±0.2	19.5±1.0
	D	33.0±1.4	30.1±0.8	30.0±0.5	29.3±1.8	30.7±1.9	30.6±0.4	29.7±1.2	29.7±0.7
Mo	B	1.5±0.5	1.3±0.5	1.8±0.5	2.8±0.7	1.5±0.5	2.7±0.3	2.0±0.4	1.8±0.2
	D								
Nb	B	29.6±0.9	30.8±1.6	28.3±1.1	30.3±1.6	28.0±1.9	30.3±1.4	28.5±0.7	27.8±0.8
	D	15.4±1.3	17.6±3.8	17.5±1.0	16.2±1.0	15.7±2.5	17.2±0.3	17.7±1.3	17.5±0.7
Ta	B	22.1±2.5	16.4±1.3	15.2±0.3	17.6±1.4	15.4±1.3	16.6±0.9	16.2±0.4	16.9±0.7
	D	6.9±0.6	7.8±4.2	7.9±0.6	7.2±0.9	7.2±0.4	7.2±0.3	8.7±1.4	8.4±0.4
Ti	B	23.3±2.5	25.1±1.9	26.1±1.6	27.0±1.5	29.3±1.1	26.3±1.0	28.2±0.4	26.6±1.5
	D	14.8±1.0	15.4±0.4	14.7±0.7	15.5±1.7	15.2±1.3	14.1±0.3	15.9±1.6	14.8±0.4
Zr	B	6.0±0.8	6.4±0.4	7.5±0.3	5.1±0.8	7.6±2.3	8.3±3.9	6.5±0.4	8.2±1.7
	D	29.7±0.9	29.1±1.0	29.8±2.0	31.7±1.6	31.2±2.0	31.1±0.3	27.8±3.2	29.7±0.9

**Figure 11.** EDS line scans of the FAST sample sintered at 1400°C for 30 min (S7).

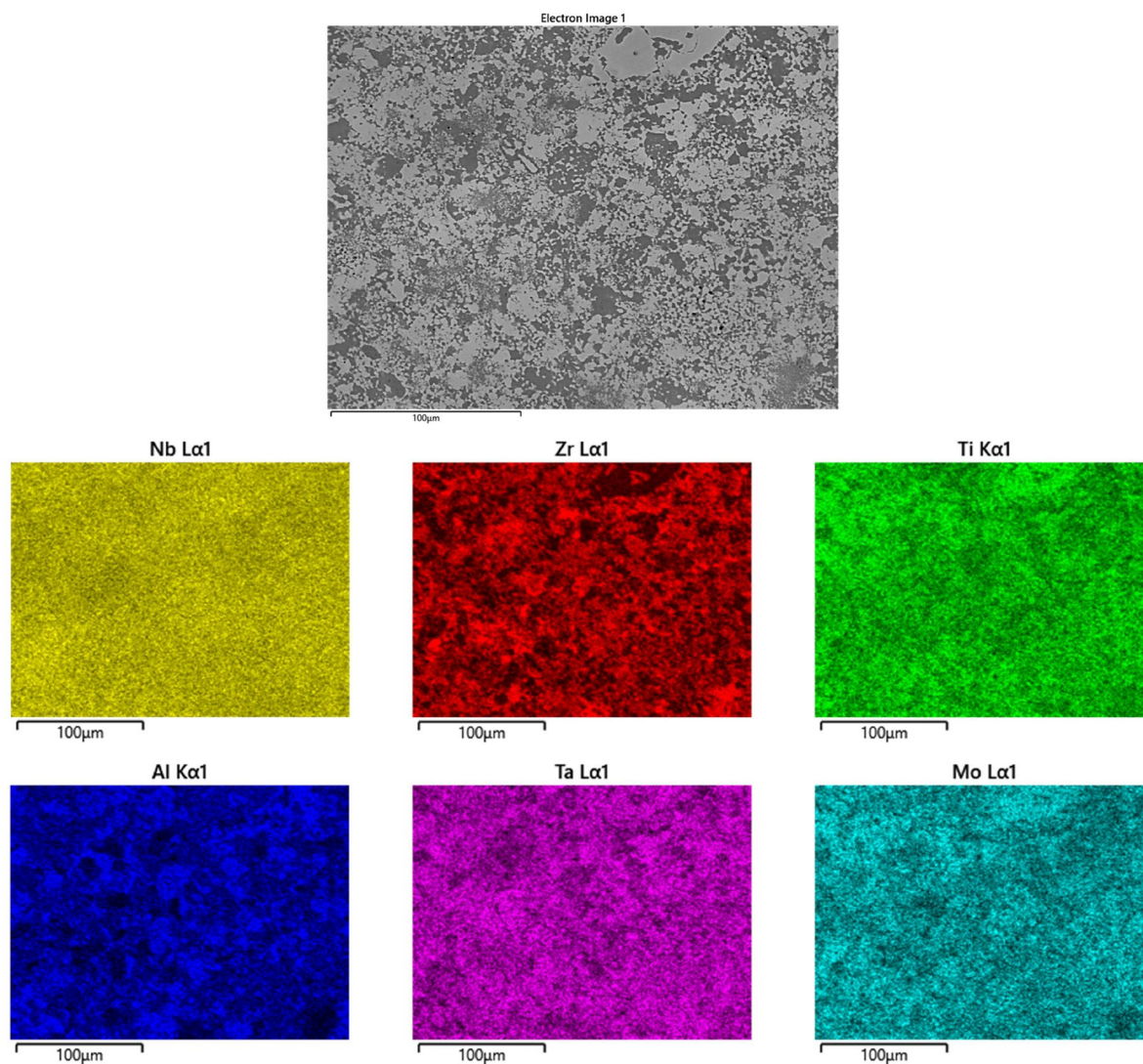
To further illustrate this, EDS line scans were taken across the interface of these two phases in S7 as shown in Figure 11. When moving across the interface: 1) The amount of Nb, Ta and Ti remained rather constant. 2) The level of Zr dropped drastically in the bright phase. 3) The level of Al also dropped in the dark phase but not as much as Zr. To support these conclusions, an EDS elemental map was also constructed as shown in Figure 12, where darker region contains more Zr and Al.

Figure 13 shows high magnification BSE-SEM micrographs of the samples sintered at 1400 and 1500°C with 15 minutes holding time. In both images, it seems that the bright phase was overlaid upon the dark phase. Interestingly, blocks/globules of the dark phases with size of about 1 to 2 μm were noted in the microstructure. In addition to that, micropores with sizes less than 1 μm were also observed in the microstructure.

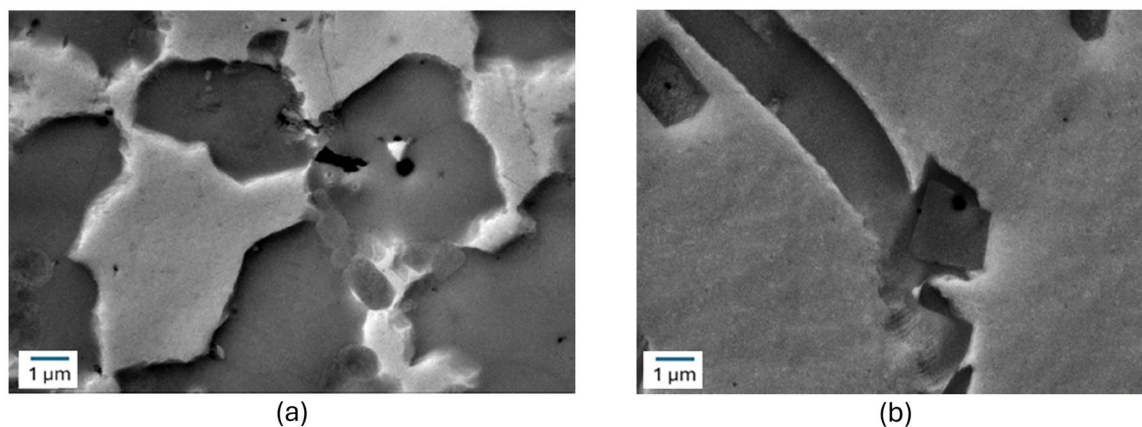
Previous works Senkov et al. (2014; 2016; 2018) show the presence of a BCC/B2 phase in alloys with similar chemical compositions prepared by the vacuum arc melting route. However, in the alloys studied here no such short-range ordering of BCC and B2 phases were seen.

### 3.5. Hardness

Hardness testing was conducted exclusively on samples sintered at 1400°C and 1500°C, owing to their relatively low porosity compared to those processed at other temperatures. The microhardness



**Figure 12.** EDS elemental maps of the FAST sample sintered at 1400 °C (S11).

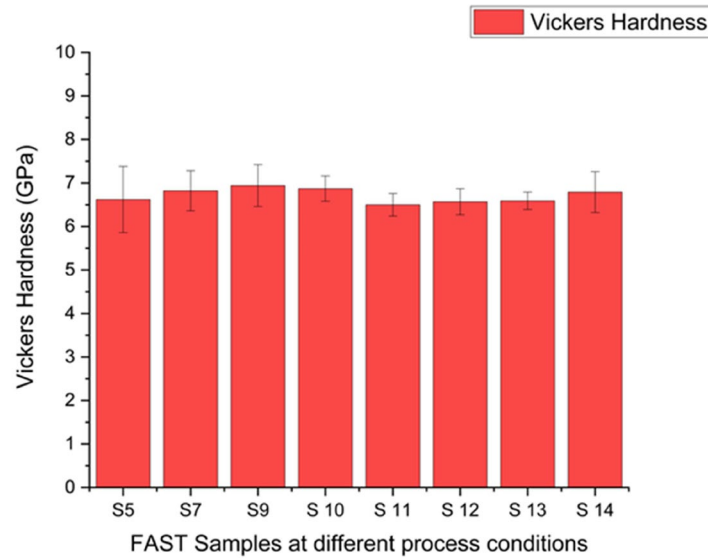


**Figure 13.** High magnification BSE-SEM micrographs of the samples a) sintered at 1400 °C (S12) b) sintered at 1500 °C (S14) (Processing details are given in Table 2).

results for samples S5 to S14 are listed in Table 5 and presented in a bar chart in Figure 14. The measured hardness values ranged from approximately 6.50 to 6.94 GPa. Variations in heating rate, cooling rate, and dwell time, as outlined in Table 2, did not result in significant differences in

**Table 5.** Vickers Hardness of the samples processed at 1400 and 1500 °C. Samples S5 to S9 were cooled in an uncontrolled manner with an uneven cooling rate of nearly 200 °C/min (uncontrolled cooling).

Sample	Temperature (°C)	Holding Time (min)	Heating Rate (°C/min)	Cooling Rate (°C/min)	Hardness (HV0.2) GPa
S5	1400	15	100	Uncontrolled	6.62 ± 0.76
S7	1400	30	100	Uncontrolled	6.82 ± 0.46
S9	1500	15	100	Uncontrolled	6.94 ± 0.48
S 10	1400	15	30	30	6.87 ± 0.29
S 11	1400	15	30	50	6.50 ± 0.26
S 12	1400	15	100	30	6.57 ± 0.30
S 13	1500	15	100	30	6.59 ± 0.20
S 14	1500	15	100	100	6.79 ± 0.47

**Figure 14.** Hardness of FAST processed AlMoNbTaTiZr alloy samples at different processing conditions.

hardness. This observation is consistent with the lack of notable microstructural changes among samples processed at 1400 °C and 1500 °C under the different parameter sets; nevertheless, it appears that increased cooling rates have resulted in higher hardness values. This phenomenon may be linked to the formation of a greater number of intermetallic compounds, necessitating further analysis of phase formation.

Although the effect of cooling rate on the densification was not quantified in this work, it is important to highlight that, as indicated by the findings presented in Table 5, increased cooling rates result in elevated hardness values in the FAST-processed samples.

For comparison, similar alloys synthesized via vacuum arc melting have been reported to exhibit hardness values in the range of 5.0 to 5.8 GPa (Senkov et al., 2018). The relatively higher hardness observed in the current study may be attributed to the finer and more homogeneous distribution of phases, along with an increased fraction of the intermetallic hexagonal phase of  $\text{Al}_3\text{Zr}_5$ .

#### 4. Conclusions

1. This work used an AlMoNbTaTiZr RHEA powder produced via a solid-state powder route (FFC Cambridge process), for the first time, to sustainably manufacture samples that could potentially be used for high temperature applications. To assess samples integrity and optimise the processing conditions, microstructural observation and microhardness testing were undertaken and reported here.

2. The studied AlMoNbTaTiZr RHEA powder consolidated using FAST technique had the maximum density when processed at temperatures above 1400 °C, above which there was minimal reduction or no change to the relative density.
3. XRF investigation in powder format and after FAST showed no loss of elements and no oxygen entrapment during the sintering process. This demonstrates the potential of FAST to manufacture samples with minimal contamination from the FFC Cambridge RHEA powder.
4. Among the process parameters, i.e. processing temperature, holding or isothermal dwell time at temperature, heating and cooling rates, the consolidation temperature had a more profound effect on density.
5. When the material was processed at consolidation temperatures above 1400 °C a microstructure of BCC matrix and hexagonal intermetallic precipitates of Al<sub>3</sub>Zr<sub>5</sub> was formed.
6. Overall, this study found that a sintering temperature of 1400 °C, a dwell time of 15 minutes, a heating rate of 100 °C/min and a cooling rate of 30 °C/min were the optimum operating conditions to produce a fine and dense consolidated part.

## Acknowledgements

The authors gratefully acknowledge Mohamed Arshad and Mohamed Amer from Coventry University for their assistance with the X-ray diffraction experiments.

## Disclosure statement

No potential conflict of interest was reported by the author(s).

## Funding

This work is part of a PhD work supported by Coventry University, under a fully funded PhD studentship: Trailblazers. The authors would like to acknowledge the support of the Henry Royce Institute for advanced materials for **DX** through the Student Equipment Access Scheme enabling access to **FCT HP D25** at **The Royce Discovery Centre at the University of Sheffield**; EPSRC Grant Number EP/R00661X/1 & EP/P02470X/1. They also acknowledge the use of the Polymer Characterisation and X-Ray Diffraction Research Technology Platforms (RTPs) at the University of Warwick, with access provided by the Warwick Analytical Science Centre (WASC) seedcorn scheme (EP/V007688/1). Finally, the authors acknowledge Metalysis Ltd. for supply of material.

## Data availability statement

Data will be made available on request.

## References

- ASTM E 799-03. (2020). Standard practice for determining data criteria and processing for liquid drop size analysis. ASTM International. <https://doi.org/10.1520/E0799-03R20E01>.
- ASTM E384-22. (2022). *Standard test method for microindentation hardness of materials*. ASTM International.
- Bhagat, R., Jackson, M., Inman, D., & Dashwood, R. (2008). The Production of Ti-Mo alloys from mixed Oxide precursors via the FFC Cambridge process. *Journal of The Electrochemical Society*, 155(6), E63. <https://doi.org/10.1149/1.2904454>
- Cavaliere, P., Sadeghi, B., & Shabani, A. (2019). Spark plasma sintering: Process fundamentals. In P. Cavaliere (Ed.), *Spark plasma sintering of materials* (pp. 3–20). Springer. [https://doi.org/10.1007/978-3-030-05327-7\\_1](https://doi.org/10.1007/978-3-030-05327-7_1)
- Chen, B., & Zhuo, L. (2023). Latest progress on refractory high entropy alloys: Composition, fabrication, post processing, performance, simulation and prospect. *International Journal of Refractory Metals and Hard Materials*, 110, 105993. <https://doi.org/10.1016/j.ijrmhm.2022.105993>
- Chen, G. Z. (2013). Forming metal powders by electrolysis. In I. Chang, & Y. Zhao (Eds.), *Woodhead publishing series in metals and surface engineering, advances in powder metallurgy* (pp. 19–41). Woodhead Publishing. <https://doi.org/10.1533/9780857098900.1.19>



- Chen, G. Z., & Fray, D. J. (2020). Invention and fundamentals of the FFC Cambridge process. In Z. Z. Fang, F. H. Froes, & Y. Zhang (Eds.), *Extractive metallurgy of titanium* (pp. 227–286). Elsevier. <https://doi.org/10.1016/B978-0-12-817200-1.00011-9>
- Dangwal, S., & Edalati, K. (2025). Developing a single-phase and nanograined refractory high-entropy alloy ZrHfNbTaW with ultrahigh hardness by phase transformation via high-pressure torsion. *Journal of Alloys and Compounds*, 1010, 178274. <https://doi.org/10.1016/j.jallcom.2024.178274>
- Diouf, S., & Molinari, A. (2012). Densification mechanisms in spark plasma sintering: Effect of particle size and pressure. *Powder Technology*, 221, 220–227. <https://doi.org/10.1016/j.powtec.2012.01.005>
- Falodun, O. E., Obadele, B. A., Oke, S. R., Olubambi, P. A., & Westraadt, J. (2019). Characterization of spark plasma sintered TiN nanoparticle strengthened titanium alloy using EBSD and TKD. *Materials Research Bulletin*, 117, 90–95. <https://doi.org/10.1016/j.materresbull.2019.04.031>
- Ferreirós, P. A., von Tiedemann, S. O., Parkes, N., Gurah, D., King, D. J. M., Norman, P., Gilbert, M.R., Knowles, A. J. (2023). VNbCrMo refractory high-entropy alloy for nuclear applications. *International Journal of Refractory Metals and Hard Materials*, 113, 106200. <https://doi.org/10.1016/j.ijrmhm.2023.106200>
- Guillon, O., Gonzalez-Julian, J., Dargatz, B., Kessel, T., Schiering, G., Räthel, J., & Herrmann, M. (2014). Field-assisted sintering technology/spark plasma sintering: Mechanisms, materials, and technology developments. *Advanced Engineering Materials*, 16(7), 830–849. <https://doi.org/10.1002/adem.201300409>
- Hu, K., Li, X., Qu, S., & Li, Y. (2013). Effect of heating rate on densification and grain growth during spark plasma sintering of 93W-5.6Ni-1.4Fe heavy alloys. *Metallurgical and Materials Transactions A*, 44(9), 4323–4336. <https://doi.org/10.1007/s11661-013-1789-5>
- Khan, M. A., Brechtel, J., Hamza, M., Feng, C. S., Mansoor, A., Jabar, B., Liaw, P.K., Affi, M. A. (2024). Influence of high-strain-rate compression and subsequent heat treatment on (TiNbZr)<sub>89</sub>(AlTa)<sub>11</sub> refractory high-entropy alloys: Dynamic-mechanical behavior and microstructural changes. *Materials and Design*, 243, 113062. <https://doi.org/10.1016/j.matdes.2024.113062>
- King, D. J. M., Middleburgh, S. C., McGregor, A. G., & Cortie, M. B. (2016). Predicting the formation and stability of single phase high-entropy alloys. *Acta Materialia*, 104, 172–179. <https://doi.org/10.1016/j.actamat.2015.11.040>
- Martin, P., Aguilar, C., & Cabrera, J. M. (2024). A review on mechanical alloying and spark plasma sintering of refractory high-entropy alloys: Challenges, microstructures, and mechanical behavior. *Journal of Materials Research and Technology*, 30, 1900–1928. <https://doi.org/10.1016/j.jmrt.2024.03.205>
- Moschetti, M., Burr, P. A., Obbard, E., Kruzic, J. J., Hosemann, P., & Gludovatz, B. (2022). Design considerations for high entropy alloys in advanced nuclear applications. *Journal of Nuclear Materials*, 567, 153814. <https://doi.org/10.1016/j.jnucmat.2022.153814>
- NRC Draft REGULATORY GUIDE DG-1263. (2014). Establishing analytical limits for zirconium based alloy cladding. ML 12284A323. <https://www.nrc.gov/docs/ML1228/ML12284A323.pdf>
- Nuclear Energy Agency. (2023). Nuclear Energy Agency, summary report of the high entropy alloys for nuclear applications workshop. 19–21. October 2021, NEA/NSC/R 9. [https://www.oecd-neo.org/upload/docs/application/pdf/2024-03/nea\\_nsc\\_r\\_2023\\_9.pdf](https://www.oecd-neo.org/upload/docs/application/pdf/2024-03/nea_nsc_r_2023_9.pdf)
- Senkov, O. N., Isheim, D., Seidman, D. N., & Pilchak, A. L. (2016). Development of a refractory high entropy superalloy. *Entropy*, 18(3), 102–e18030102. <https://doi.org/10.3390/e18030102>
- Senkov, O. N., Jensen, J. K., Pilchak, A. L., Miracle, D. B., & Fraser, H. L. (2018). Compositional variation effects on the microstructure and properties of a refractory high-entropy superalloy AlMo<sub>0.5</sub>NbTa<sub>0.5</sub>TiZr. *Materials and Design*, 139, 498–511. <https://doi.org/10.1016/j.matdes.2017.11.033>
- Senkov, O. N., Miracle, D. B., Chaput, K. J., & Couzinie, J. P. (2018). Development and exploration of refractory high entropy alloys - A review. *Journal of Materials Research*, 33(19), 3092–3128. <https://doi.org/10.1557/jmr.2018.153>
- Senkov, O. N., Senkova, S. V., & Woodward, C. (2014). Effect of aluminum on the microstructure and properties of two refractory high-entropy alloys. *Acta Materialia*, 68, 214–228. <https://doi.org/10.1016/j.actamat.2014.01.029>
- Senkov, O. N., Wilks, G. B., Miracle, D. B., Chuang, C. P., & Liaw, P. K. (2010). Refractory high-entropy alloys. *Intermetallics*, 18(9), 1758–1765. <https://doi.org/10.1016/j.intermet.2010.05.014>
- Technical Note TN156. (2021). Results Interpretation, HORIBA Scientific, Understanding and interpreting particle size distribution calculations. [https://static.horiba.com/fileadmin/Horiba/Products/Scientific/Particle\\_Characterization/Downloads/Technical\\_Notes/TN156\\_Understanding\\_and\\_Interpreting\\_PSD\\_Calculations.pdf](https://static.horiba.com/fileadmin/Horiba/Products/Scientific/Particle_Characterization/Downloads/Technical_Notes/TN156_Understanding_and_Interpreting_PSD_Calculations.pdf)
- Wang, X. D., Bai, W. L., Zhang, Z., Wang, Z. B., & Ren, X. C. (2024). Enhancing fatigue resistance of high-entropy alloy by designing a hierarchically heterogeneous microstructure. *Journal of Materials Research and Technology*, 33, 673–682. <https://doi.org/10.1016/j.jmrt.2024.09.091>
- Weston, N. S., Derguti, F., Tudball, A., & Jackson, M. (2015). Spark plasma sintering of commercial and development titanium alloy powders. *Journal of Materials Science*, 50(14), 4860–4878. <https://doi.org/10.1007/s10853-015-9029-6>

- Whitfield, T. E., Pickering, E. J., Owen, L. R., Senkov, O. N., Miracle, D. B., Stone, H. J., & Jones, N. G. (2021a). An assessment of the thermal stability of refractory high entropy superalloys. *Journal of Alloys and Compounds*, 857, 157583. <https://doi.org/10.1016/j.jallcom.2020.157583>
- Whitfield, T. E., Stone, H. J., Jones, C. N., & Jones, N. G. (2021b). Microstructural degradation of the AlMo0.5NbTa0.5TiZr refractory metal high-entropy superalloy at elevated temperatures. *Entropy*, 23(1), 80. <https://doi.org/10.3390/e23010080>
- Xiong, W., Guo, A. X. Y., Zhan, S., Liu, C. T., & Cao, S. C. (2023). Refractory high-entropy alloys: A focused review of preparation methods and properties. *Journal of Materials Science and Technology*, 142, 196–215. <https://doi.org/10.1016/j.jmst.2022.08.046>
- Yousefian, C. B., Magnussen, J. P., Lloyd, M. J., Ma, K., Wilcox, H., Cackett, A. J., & Knowles, A. J. (2025). Zr35Ti35Nb20V5Al5 refractory high entropy alloy designed for low-density, high specific strength and ductility. *Scripta Materialia*, 265, 116733. <https://doi.org/10.1016/j.scriptamat.2025.116733>
- Zhang, B., Huang, Y., Dou, Z., Wang, J., & Huang, Z. (2024). Refractory high-entropy alloys fabricated by powder metallurgy: Progress, challenges and opportunities. *Journal of Science: Advanced Materials and Devices*, 9(2), 100688. <https://doi.org/10.1016/j.jsamd.2024.100688>